Journal of Physics D: Applied
Physics

PAPER

Investigation of hybridized bluff bodies for flow-induced vibration energy harvesting

To cite this article: Junlei Wang *et al* 2022 *J. Phys. D: Appl. Phys.* **55** 484001

IOP Publishing Journal of Physics D: Applied Physics

J. Phys. D: Appl. Phys. **55** (2022) 484001 (10pp) https://doi.org/10.1088/1361-6463/ac928e

Investigation of hybridized bluff bodies for flow-induced vibration energy harvesting

Junlei Wang[1], **Yiqing Wang**[1] and **Guobiao Hu**[2,*]

[1] School of Mechanical and Power Engineering, Zhengzhou University, Zhengzhou 450000, People's Republic of China
[2] School of Civil and Environmental Engineering, Nanyang Technological University, Singapore

E-mail: guobiao.hu@ntu.edu.sg

Received 3 July 2022, revised 14 September 2022
Accepted for publication 16 September 2022
Published 7 October 2022

Abstract

Small-scale wind energy harvesting based on flow-induced vibration (FIV) mechanisms has attracted lots of research interest in recent years. Vortex-induced vibration (VIV) and galloping energy harvesters usually outperform each other in different wind-speed ranges. To combine the advantages of VIV and galloping harvesters, this paper explores the idea of using a hybridized bluff body constituting of two cylindrical and one cuboid segment for wind energy harvesting. The total length of the hybridized bluff body was fixed. The cuboid segment length was varied to investigate the effect on the FIV behavior of the bluff body. The results show that, when the cuboid segment is short in length, the bluff body exhibits VIV-like behavior in the low wind-speed range and galloping-like behavior in the high-speed range. In the medium wind-speed range, galloping-VIV coupling appears. However, if the cuboid segment is longer, the galloping-VIV coupling phenomenon disappears; the hybridized bluff body behaves just like a cuboid one and only exhibits a galloping motion. In addition to experiments, computational fluid dynamics (CFD) simulations are also conducted to provide more insights into the aerodynamics of the hybridized bluff body. The simulation results reveal that introducing hybridization into the bluff body changes the vorticity flow behind it and alters the vortex-shedding behavior. The vortex-shedding effect, in turn, affects the vibration of the bluff body, as well as the performance of the harvester.

Keywords: flow-induced vibration, energy harvesting, galloping-VIV coupling, piezoelectric

(Some figures may appear in color only in the online journal)

1. Introduction

With the development of society, global energy use is ever-growing rapidly. The decline of non-renewable energy reserves urges people to seek sustainable energy resources to ease the pressure of energy demands [1–3]. Many researchers have been working on renewable energy technology and have produced considerable achievements [4–6]. Nowadays, wind, solar, ocean, and many other types of clean energy have been exploited, and corresponding energy-generation systems have been developed [7–9]. Several kinds of clean energy-generation systems, such as solar cell panels and wind turbines, have been widely implemented for practical applications in our daily life. Large-scale wind turbines can produce sufficient power for industrial electricity and commercial purposes. In addition, small-scale wind energy harvesting technology has also been proposed to replace the electrical batteries of low-power-consumption electronic devices [10, 11]. Unlike bulky wind turbines that are designed based on the rotation mechanism, most small-scale wind energy harvesters are designed based on flow-induced vibration (FIV)

---

[*] Author to whom any correspondence should be addressed.

mechanisms to realize miniature dimensions [12, 13]. FIV phenomena are usually caused by aerodynamic instability under the vortex-shedding effect induced by fluid passing through slender structures. FIV commonly leads to damage and destruction of engineering structures. One famous example is the collapse of the Tacoma bridge [14].

From the perspective of energy harvesting, there exists the potential to convert hydrodynamic energy into electricity. Since wind and water flows exist widely in our daily life, FIV energy harvesting is a promising prospect. According to the underlying mechanisms, FIV can be further classified into vortex-induced vibration (VIV) [15–17], galloping [18–20], flutter [21, 22], buffeting [12], and their combinations. By adopting different energy-conversion mechanisms, FIV energy harvesters can be designed using electromagnetic [23], piezoelectric [24–26], dielectric [27], and triboelectric [27–29] transductions.

Piezoelectric materials have high-power densities and can be easily integrated with mechanical structures. Thus, using piezoelectric materials to realize FIV energy harvesting has attracted enormous research interest [30–32]. An FIV piezoelectric energy harvester (PEH) can be obtained by attaching a bluff body at the free end of a cantilever beam. Once the FIV-PEH is placed in a flow field with a sufficiently high flow speed, FIVs may occur, and electrical power can then be produced [33–35]. Considering the cut-in wind speed, the start-oscillation condition, and the structural design complexity, VIV and galloping harvesters are pretty efficient in harnessing energy from wind flows [36, 37].

Most of the VIV-PEHs reported in the existing literature adopted cylindrical bluff bodies. VIV has a unique lock-in phenomenon when the vortex-shedding frequency is close to its natural frequency. Within the lock-in region, i.e. a wind-speed range, the VIV system carries on large-amplitude vibrations [38, 39]. The lock-in phenomenon of VIV usually occurs at low wind speeds. Thus, it has been exploited for energy harvesting. However, with the further increase of wind speed, the efficiency of a VIV-PEH degrades severely. Wang *et al* [40] designed a cylindrical bluff body with Y-shaped attachments and discussed their influences on wind energy harvesting. The results showed that Y-shaped attachments could lead the cylindrical bluff body to transition from VIV to galloping, thus improving energy-harvesting efficiency. Wang *et al* [41] investigated the effect of adding a small rectangular plate behind a cylinder on wind energy harvesting. A transformation from VIV to galloping was observed by changing the size and position of the rectangular plate, resulting in the reinforcement of efficiency compared to conventional VIV-PEHs. Wang *et al* [42] studied the influences of the installation angles of a couple of splitters on a VIV-PEH. About 60° was determined to be the optimal installation angle to realize VIV-to-galloping transformation. The maximum voltage produced by the optimized wind energy harvester could reach 1.85 times that of a VIV-PEH.

Unlike the lock-in phenomenon of VIV, the vibration intensity of a galloping system monotonically increases with the wind-speed increase. However, galloping normally occurs when a bluff body with sharp corners is under a moderate to high wind flow [19, 43–45]. In other words, the cut-in wind speed of a galloping system is usually high, making it not suitable for low wind-speed energy harvesting. Therefore, most research about PEHs has mainly focused on lowering the cut-in wind speed. Wang *et al* [46] used bluff bodies with butterfly- and spindle-like sections to design FIV-PEHs. They studied the effects of the width ratios and installation directions of the bluff bodies on FIV energy harvesting. The results showed that the vibration of the vertically installed spindle-like bluff body evolved from VIV to galloping and exhibited an evident coupling between VIV and galloping. The threshold speed was significantly lower than that of a traditional cuboid bluff body. Tan *et al* [47] studied the influences of three bluff bodies, respectively, with semi-circular, triangular, and trapezoid sections on galloping energy harvesting. The test results revealed that the threshold speed of the trapezoid bluff body was much lower than that of the two others. Although the trapezoid bluff body did not exhibit coupling between VIV and galloping, the output voltage of the corresponding harvester was always larger compared to the other two counterparts. Zhao *et al* [48] developed a new funnel-shaped bluff body and compared it with rectangular and triangular bluff bodies for wind energy harvesting. The experimental results validated the superior performance of the funnel-shaped bluff body in energy harvesting applications: not only the cut-in wind speed was reduced, but also the output voltage was significantly increased.

Inspired by the idea of coupling VIV and galloping, this paper proposes a novel bluff body by hybridizing a cuboid (usually used to induce galloping) and a cylinder (usually used to induce VIV). The rest of the paper is organized as follows. Section 2 provides an overview of the proposed FIV-PEH, including the design concept and geometries of the bluff bodies. The experimental setup and the computational fluid dynamics (CFD) simulation model are explained. The experimental and simulation results and discussions are presented in sections 3 and 4. In the last section, i.e. section 5, conclusions of the work presented in this paper are summarized.

2. Design, experiment, and simulation

2.1. Design concept

Different bluff body shapes will cause different FIV phenomena, such as galloping, VIV, or the coupling of galloping and VIV. In terms of applications in energy harvesting, galloping has a good performance at high wind speeds, while VIV can more easily occur at low wind speeds. To inherit the advantages of both galloping and VIV, we propose hybridizing cuboid and cylindrical bluff bodies with the expectation that this hybridized bluff body will exhibit a low cut-in wind speed and good performance at high wind speeds. A schematic of the proposed FIV-PEH using the hybridized bluff body is shown in figure 1. The hybridized bluff body consists of one cuboid segment in the middle and two symmetrical cylindrical segments connected to the cuboid segment on two sides. The diameter of the cylinder is D. The cross-section of the cuboid segment is a square with a side length of D as well. In addition

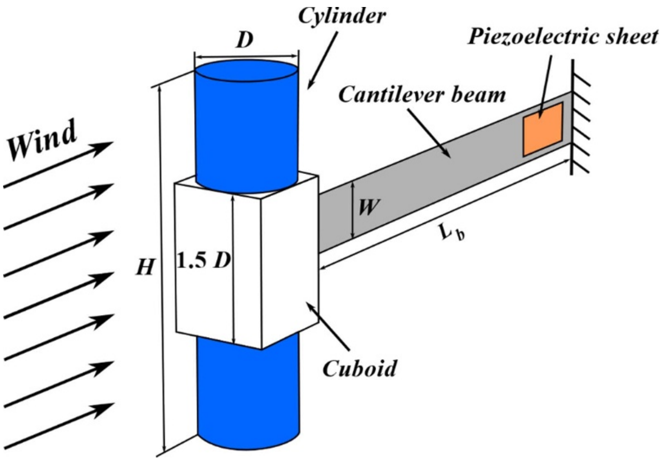

Figure 1. Schematic of the proposed FIV-PEH using a hybridized bluff body.

to the hybridized bluff body, the proposed FIV-PEH consists of a cantilever beam and a piezoelectric transducer. One end of the cantilever beam is clamped. The other end is attached to the hybridized bluff body. The piezoelectric sheet is bonded at the clamped end of the cantilever beam. In the study, we will change the hybridization rate, i.e. vary the length of the cuboid segment (L) and keep the lengths of the two cylindrical segments untouched, to investigate its influence on the energy-harvesting performance of the proposed FIV-PEH. Two FIV-PEHs that are, respectively, mounted with the conventional cuboid and cylindrical bluff bodies will be used as baseline models for later comparison.

2.2. Experimental setup

The fabricated FIV-PEHs and the experimental setup are shown in figure 2. In the experiment, the FIV-PEH prototype was placed in a wind tunnel with a diameter of 0.4 m. A draught fan was installed at one end of the wind tunnel to produce suction wind flow. At the other end of the wind tunnel, honeycombs were installed to stabilize the suction wind flow. The bluff bodies were made of rigid foam, and the masses of all bluff bodies were controlled near 2.7 g. The height of the whole bluff body, i.e. H, and the diameter of the cylindrical segment, i.e. D, were 118 mm and 32 mm, respectively. The length L_b, width W, and thickness h_b of the aluminum cantilever beam were 200 mm, 20 mm, and 0.3 mm, respectively. The cantilever beam was made of aluminum with a nominal mass density of 2700 kg m^{-3} and Young's modulus of 70 GPa. The piezoelectric sheet with the dimensions of 30 mm × 20 mm × 0.5 mm was bonded near the clamped end of the cantilever beam. The piezoelectric sheet was made of lead zirconate titanate (PZT-5) with a capacitance C_p of 30.8 nF.

Despite the hybridization treatment, the overall geometric dimensions of the proposed FIV-PEHs, especially the piezoelectric cantilever beam, were almost identical to those of the baseline models. To investigate the hybridization rate effect on the aerodynamics of the proposed FIV-PEH, we varied the length of the cuboid segment. Figures 2(a)–(f) show the hybridized FIV-PEHs with cuboid segments of different lengths: 16 mm, 32 mm, 48 mm, 64 mm, 80 mm, and 96 mm. In the wind tunnel test, the wind speed was increased from 0.865 m s^{-1} to 4.29 m s^{-1}. The displacement responses and the voltage output responses were measured and recorded.

2.3. CFD model

In addition to the experiment, three-dimensional CFD analyses were carried out using the commercial software XFlow. Taking a cylindrical bluff body as an example, it is placed in a flow field, i.e. the rectangular computational domain, with a velocity of 2.646 m s^{-1}, as shown in figure 3. The length, width, and height of the computational domain are 35 D, 20 D, and 3.69 D, respectively. The left-hand side of the computational domain is set as the inlet and its right-hand side as the outlet. The surfaces of the bluff body and the remaining boundaries are set as stationary walls. The bluff body is placed 10 D away from the inlet. An external single-phase forced incompressible model is chosen to simulate the flow. The Smagorinsky turbulence model is selected to simulate the flow behavior. Table 1 lists the parameter settings of the flow field.

To determine the suitable grid resolution that can not only maintain accuracy but also reduce calculation time, we varied the grid resolution: $D/30$, $D/32$, $D/34$, $D/35$, $D/39$, and $D/50$. The number of grids is correspondingly 1234 896, 1498 504, 1959 720, 2602 008, and 5492 898. In XFlow, the time step is set as automatic. For the example bluff body, the simulation results of the drag coefficient, i.e. C_D, are presented in figure 4. It can be seen that C_D first increases by refining the grid resolution. When the lattice size reaches $D/35$, the result becomes similar to that with a further refined grid resolution of $D/39$, indicating convergence. Therefore, to strike a balance between accuracy and efficiency, the grid resolution is set to be $D/35$ in the simulation.

3. Experimental results and discussions

This section presents the experimental results of the FIV-PEHs using different hybridized bluff bodies. For brevity, hereinafter, we use 'X*D* bluff body' to refer to the hybridized bluff body with a cuboid segment length of XX. Moreover, we use 'X*D* FIV-PEH' to indicate the FIV-PEH using the XX bluff body. For instance, 0.5*D* bluff body refers to the hybridized bluff body with a cuboid segment length of 0.5*D*. And 0.5*D* FIV-PEH refers to the prototype as demonstrated in figure 2(a).

3.1. Galloping-VIV coupled cases: 0.5D and 1D FIV-PEHs

For the FIV-PEHs equipped with 0.5*D* and 1*D* bluff bodies, figure 5 presents their V_{rms} (the subscript rms denotes root mean square) and $y_{\max}$ (the displacement of the bluff body) versus wind speed. The results of the two baseline models are also provided for comparison. For brevity, 'cuboid' and 'cylinder' in the legend of figure 5 denote the two baseline models, namely, the galloping (G)-PEH and the VIV-PEH, respectively. Since the voltage is proportional to the

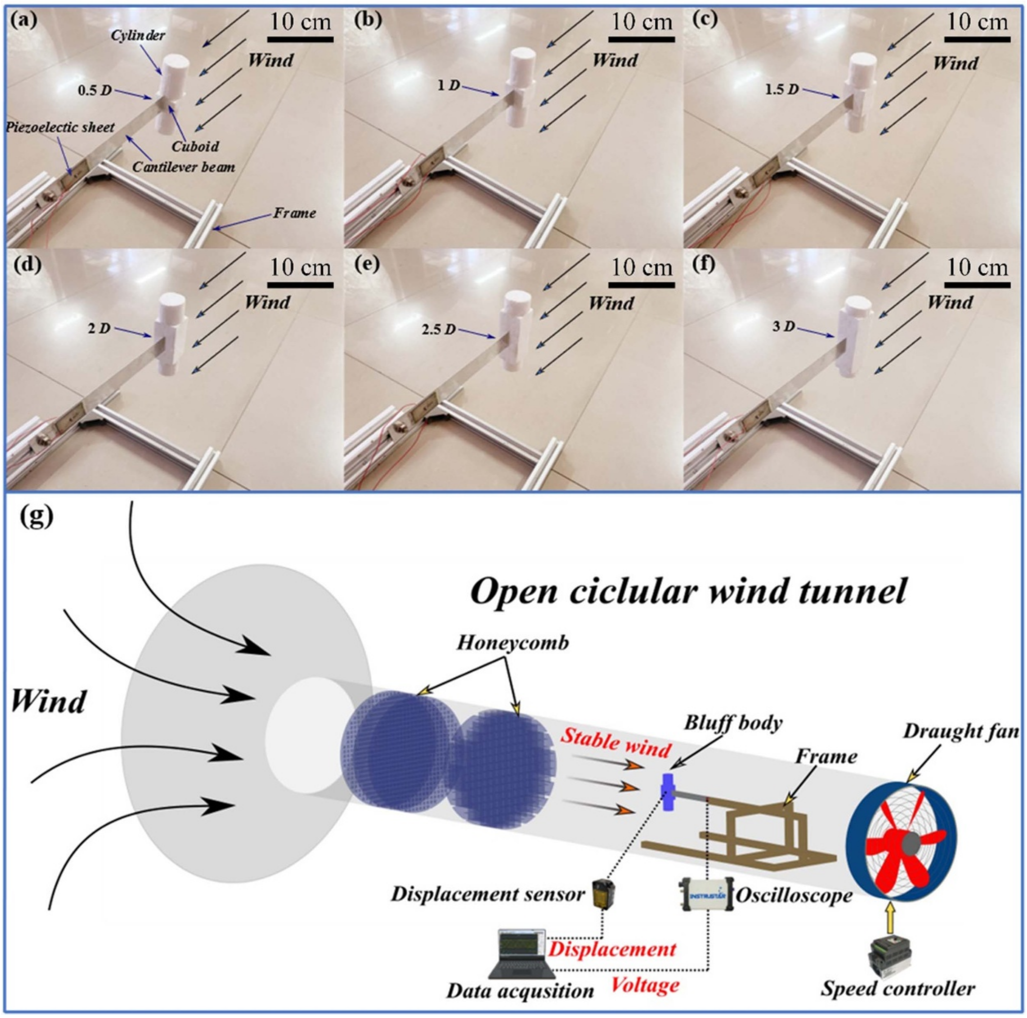

Figure 2. Fabricated FIV-PEH prototypes with different lengths of cuboid segments (a)–(f); the wind tunnel experiment setup (g).

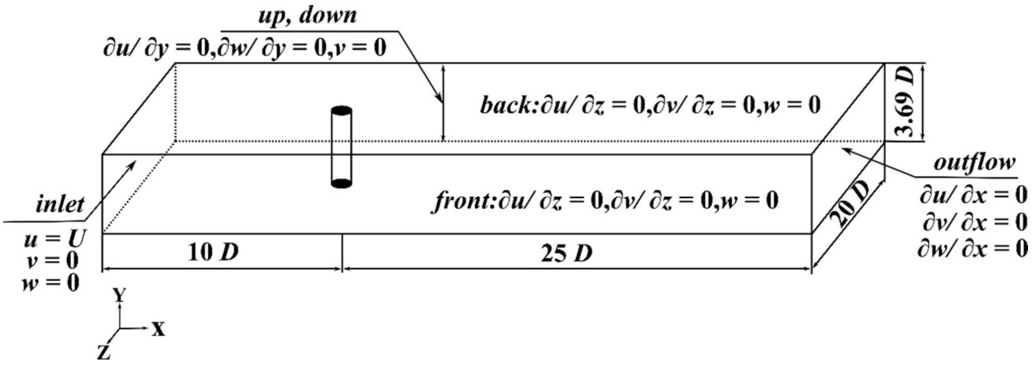

Figure 3. CFD computational domain and boundary conditions.

displacement, the evolution trends of V_{rms} and $y_{\max}$ shown in figures 5(a) and (b) are similar.

From figure 5, it is noted that the cut-in wind speed of the VIV-PEH that uses the cylindrical bluff body is about 1.55 m s^{-1}. A lock-in phenomenon is observed over a wind-speed range from 1.55 m s^{-1} to 3.19 m s^{-1}. Within the lock-in region, the VIV-PEH can produce a maximum voltage of 6.37 V at a wind speed of 2.65 m s^{-1}. The other baseline model using a cuboid bluff body, i.e. the G-PEH, exhibits typical galloping behavior: with the increase of the wind speed, both the voltage and displacement responses monotonically increase. The cut-in wind speed of the G-PEH is about 1.82 m s^{-1}, which is, as expected, higher than that of the VIV-PEH.

The dynamic responses of the 0.5*D* FIV-PEH start to increase from a wind speed of 1.687 m s^{-1} until 3.057 m s^{-1}. Then, a decline region appears from 3.057 m s^{-1} to

Table 1. Parameter settings of the flow field in XFlow.

Parameter	Value
Molecular weight	28.996 u
Reference density	1.225 kg m^{-3}
Operating temperature	288.15 K
Dynamic viscosity	1.7894×10^{-5} Pa s
Thermal conductivity	0.0243 W·(m K)$^{-1}$
Specific heat capacity	1006.43 J·(kg K)$^{-1}$

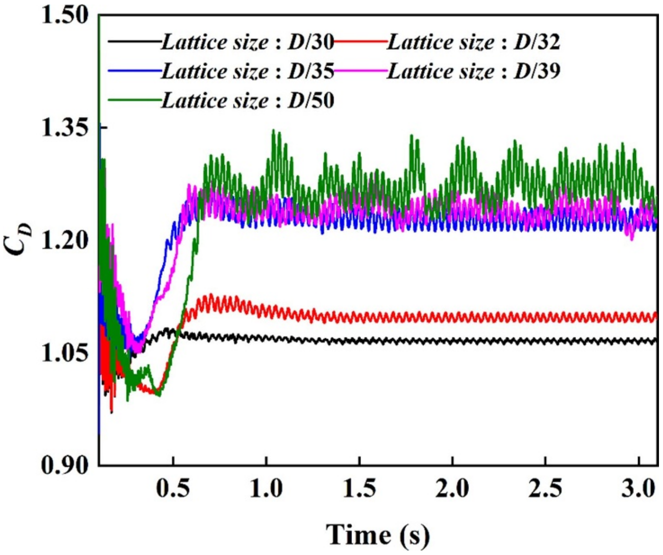

Figure 4. Time-history responses of the drag coefficient simulated by XFlow at different grid resolutions.

3.605 m s^{-1}. These characteristics resemble the behavior of VIV. The voltage output produced by the 0.5*D* FIV-PEH does not decrease but becomes relatively stable after 3.605 m s^{-1} until the end of the test. The above phenomena indicate that partial interference [49, 50] between VIV and galloping occurs in the 0.5*D* FIV-PEH. The maximum attainable voltage of the 0.5*D* FIV-PEH is about 4.8 V at a wind speed of 3.057 m s^{-1}. Compared to the two baseline models, it can be found that the voltage output from the 0.5*D* FIV-PEH is larger than that of the G-PEH between a wind speed of 1.687 m s^{-1} and 2.783 m s^{-1}, but smaller than that of the VIV-PEH between a wind speed of 1.55 m s^{-1} and 3.194 m s^{-1}. After 3.194 m s^{-1}, which is beyond the lock-in region, the voltage output from the VIV-PEH becomes nearly zero; thus, the 0.5*D* FIV-PEH outperforms it significantly. In summary, except for the wind-speed range of 2.783–3.194 m s^{-1}, the 0.5*D* FIV-PEH can outperform the G-PEH at low wind speeds and the VIV-PEH at high wind speeds.

From the results in figure 5, we can note that the overall dynamic responses of the 1*D* FIV-PEH are similar to those of the 0.5*D* FIV-PEH. The cut-in wind speed of the 1*D* FIV-PEH is also around 1.687 m s^{-1}. The voltage output amplitude first increases with the wind speed until about 3.331 m s^{-1}, then tends to decrease slightly but finally rises back to some extent. Partial interference between galloping and VIV also exists in the 1*D* FIV-PEH [49, 50]. Regarding the voltage output, the 1*D* FIV-PEH surpasses the 0.5*D* FIV-PEH substantially. Over the wind-speed range under investigation, the maximum voltage amplitude that can be produced by the 1*D* FIV-PEH is about 6.48 V, which is 1.52 times larger than that of the 0.5*D* FIV-PEH. Moreover, the 1*D* FIV-PEH is always at the intermediate level in both the low- and high-speed ranges even compared to the two baseline models. From this point of view, the 1*D* FIV-PEH is quite robust and can always produce considerable voltage output over the largest wind-speed range in the experiment. It is worth mentioning that, since the tip masses (i.e. weights of the bluff bodies) of all the FIV-PEHs are controlled to be almost the same, their angular natural frequencies (ω_n) are very close. According to the well-known formula to estimate the optimal resistance, i.e. $R_{\text{opt}} = 1/(\omega_n C_p)$, it can be easily deduced that the optimal resistances of all the FIV-PEHs should be almost the same. Therefore, it is reasonable to use the RMS voltage output to evaluate the power-generation capability since $P_{\text{avg}} = (V_{\text{rms}})^2/R$, where R represents the load resistance.

3.2. *Transitional case: 1.5*D *FIV-PEH*

We then further increased the length of the cuboid segment to see whether the aerodynamics of the hybridized bluff body can evolve to galloping to a higher degree. Figure 6 presents the results of the 1.5*D* FIV-PEH. Compared to the two baseline models, the results of the 1.5*D* FIV-PEH are much more similar to those of the VIV-PEH: (a) the cut-in wind speed is almost the same; (b) the voltage and displacement amplitude monotonically increase with the wind speed; and (c) the lock-in region phenomenon does not exist. At low wind speeds just after the threshold value, the voltage output amplitude of the 1.5*D* FIV-PEH is slightly larger than that of the G-PEH. The minor convexes that result in the enhancement on the response curve in figure 6 over the range of 1.824–3.194 m s^{-1} may be caused by the modest interference of VIV. For example, at a wind speed of 3.194 m s^{-1}, the voltage output amplitude of the 1.5*D* FIV-PEH is about 6.35 V, which indicates a 6.8% increase compared to that of the G-PEH (6.01 V). However, when the wind speed further increases beyond 3.331 m s^{-1}, the voltage amplitude produced by the 1.5*D* FIV-PEH becomes noticeably smaller than that of the G-PEH. In short, the voltage output of the 1.5*D* FIV-PEH is much smaller than that of the VIV-PEH at low wind speeds and noticeably smaller than that of the G-PEH at high wind speeds. Therefore, from a wind energy harvesting perspective, the 1.5*D* FIV-PEH is not a good design.

3.3. *Galloping cases:* 2D, 2.5D, *and* 3D *FIV-PEHs*

Will further increasing the length of the cuboid segment lead to a transition to pure galloping? More experiments were conducted to answer this question. Figure 7 presents the experimental results of 2*D*, 2.5*D*, and 3*D* FIV-PEHs. It can be seen that, with the increase of wind speed, the displacement and voltage responses of the three FIV-PEHs are quite similar to that of the G-PEH. The cut-in wind speeds of the three FIV-PEHs are also very close to that of the G-PEH, which is about

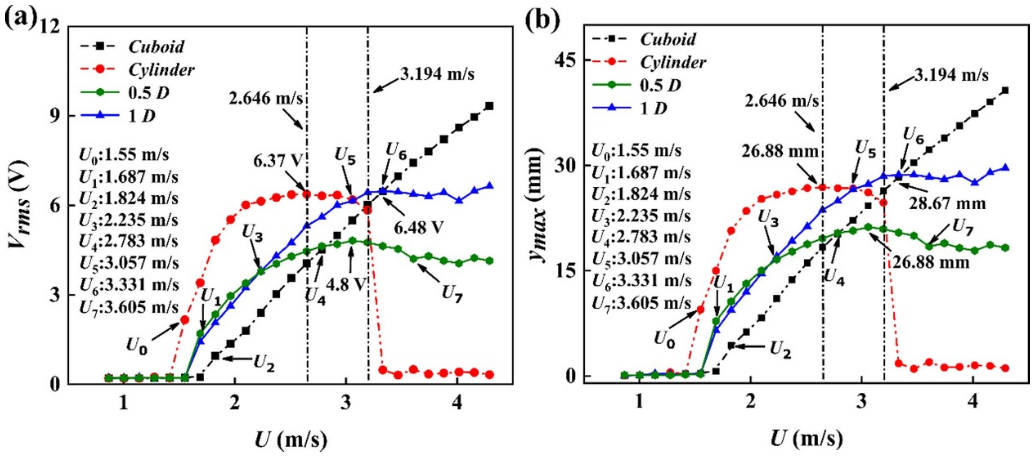

Figure 5. The experimental results of the 0.5D and 1D FIV-PEHs: (a) RMS voltage output versus wind speed; (b) displacement amplitude versus wind speed.

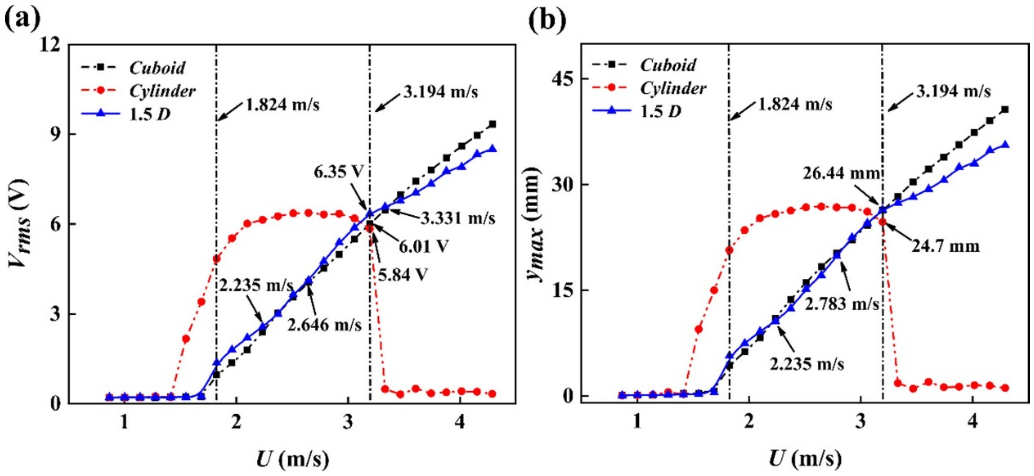

Figure 6. The experimental results of the 1.5D FIV-PEH: (a) RMS voltage output versus wind speed; (b) displacement amplitude versus wind speed.

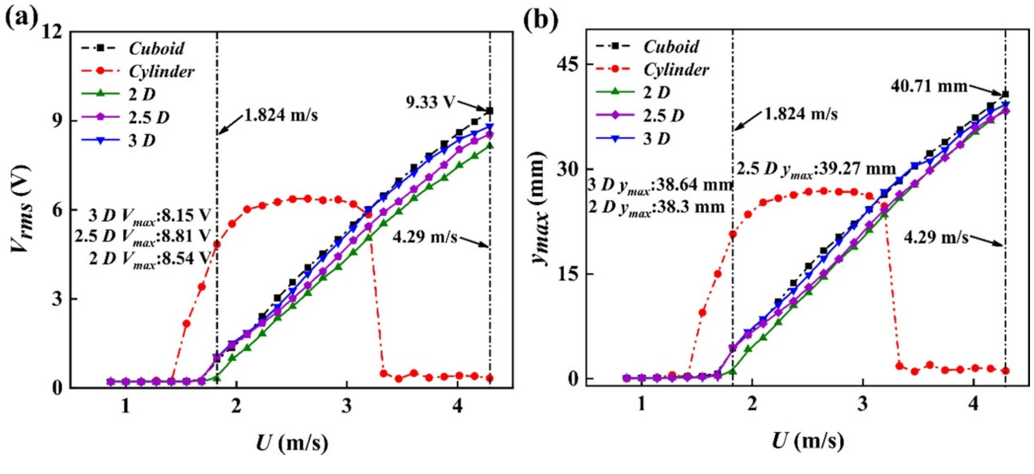

Figure 7. Experimental results of the 2D, 2.5D, and 3D FIV-PEHs: (a) RMS voltage output versus wind speed; (b) displacement amplitude versus wind speed.

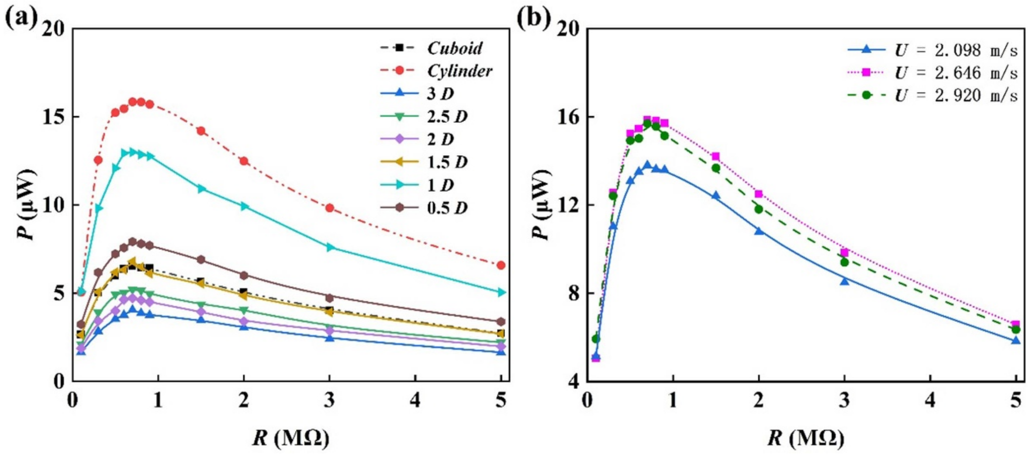

Figure 8. (a) Power output versus load resistance for different wind energy harvesters; (b) power output versus load resistance for the VIV-PEH (cylindrical bluff body) under different wind speeds.

1.824 m s^{-1}. Moreover, it is noted that, with the increase of the length of the cuboid segment, the response curves approach those of the G-PEH more closely. The curves of the 3*D* FIV-PEH become almost indistinguishable from those of the G-PEH. By referring to figure 2, we know this is because the 3*D* bluff body is already pretty similar to a pure cuboid bluff body. Among the three FIV-PEHs, the 3*D* FIV-PEH produces the largest voltage output, while the 2*D* FIV-PEH generates the smallest. At a wind speed of 4.29 m s^{-1}, they can, respectively, produce voltage outputs of 8.81 V, 8.54 V, and 8.15 V.

From the perspective of energy harvesting, we can conclude that, once the hybridized FIV-PEH is tuned beyond the transitional case, further increasing the length of the cuboid segment will only deteriorate the performance of the harvester: the voltage decreases, and the cut-in wind speed increases. However, from another perspective, the hybridized bluff body can help reduce the FIV compared to the pure cuboid one.

3.4. Power output analysis

As aforementioned, all of the bluff bodies of the FIV-PEHs are calibrated with almost the same mass, and their natural frequencies are very close. Therefore, the optimal resistances of all the FIV-PEHs should be almost the same. To validate this speculation, an experimental test was performed to determine the actual optimal resistances of the FIV-PEHs. Figure 8(a) presents the result at a wind speed of 2.646 m s^{-1}. It can be noted that, regardless of the bluff body type, all the power curves first increase, then decrease, and attain the maximum around the same resistance of about 0.7 MΩ. The power output results agree well with the predictions based on the voltage output presented in figures 5–7: within the lock-in region of the VIV-PEH, the cylindrical bluff body performs best, followed by the 1*D* bluff body. In addition, the influence of wind speed on the optimal resistance was also investigated for an example case, i.e. the VIV-PEH, and the results are presented in figure 8(b). One can easily find that, disregarding the wind-speed change, the power peak is always obtained at 0.7 MΩ. Since the optimal resistance is nearly a constant for all the FIV-PEHs in our case studies and under different wind speeds, it is confirmed that the voltage comparisons presented in previous subsections can reveal the power-generation abilities of the FIV-PEHs.

4. CFD simulation results

From the studies in the above section, we find that the 0.5*D* and 1*D* bluff bodies are the most interesting cases since they exhibit the galloping-VIV coupling phenomenon. Therefore, three-dimensional CFD simulations were carried out to provide more insights into their aerodynamics. Figure 9 provides a clear visualization of the vorticity contours behind the cuboid, cylindrical, and hybridized bluff bodies at a wind speed of 2.646 m s^{-1}. *T* stands for the vortex-shedding period. Due to some uncertainties in the installation and connection between the beam and the bluff body, the natural frequencies of the harvesters are not precisely the same but are very close, as expected, though the weights of the bluff bodies are controlled to be almost the same. According to the tests, the natural frequencies of the cylindrical, cuboid, 0.5*D*, and 1*D* FIV-PEHs are identified to be 7.24 Hz, 6.823 Hz, 7.29 Hz, and 7.18 Hz, respectively. It can be observed that the vorticity behind the cuboid bluff body is dispersed, while the vorticity flow behind the cylindrical bluff body forms an obvious vortex-shedding effect. Thus, it is unsurprising that the VIV-PEH using the cylindrical bluff body vibrates at a larger amplitude. And this also explains why the voltage output of the VIV-PEH is larger than that of the G-PEH. Behind the 0.5*D* and 1*D* bluff bodies, we can note that appreciable vortex-shedding phenomena also take place, especially compared to the dispersed vorticity behind the cuboid one. This indicates that, similar to the cylindrical bluff body, the 0.5*D* and 1*D* bluff bodies carry on VIVs.

Moreover, by carefully comparing the vorticity flows behind the 0.5*D* and 1*D* bluff bodies, that behind the 1*D* bluff

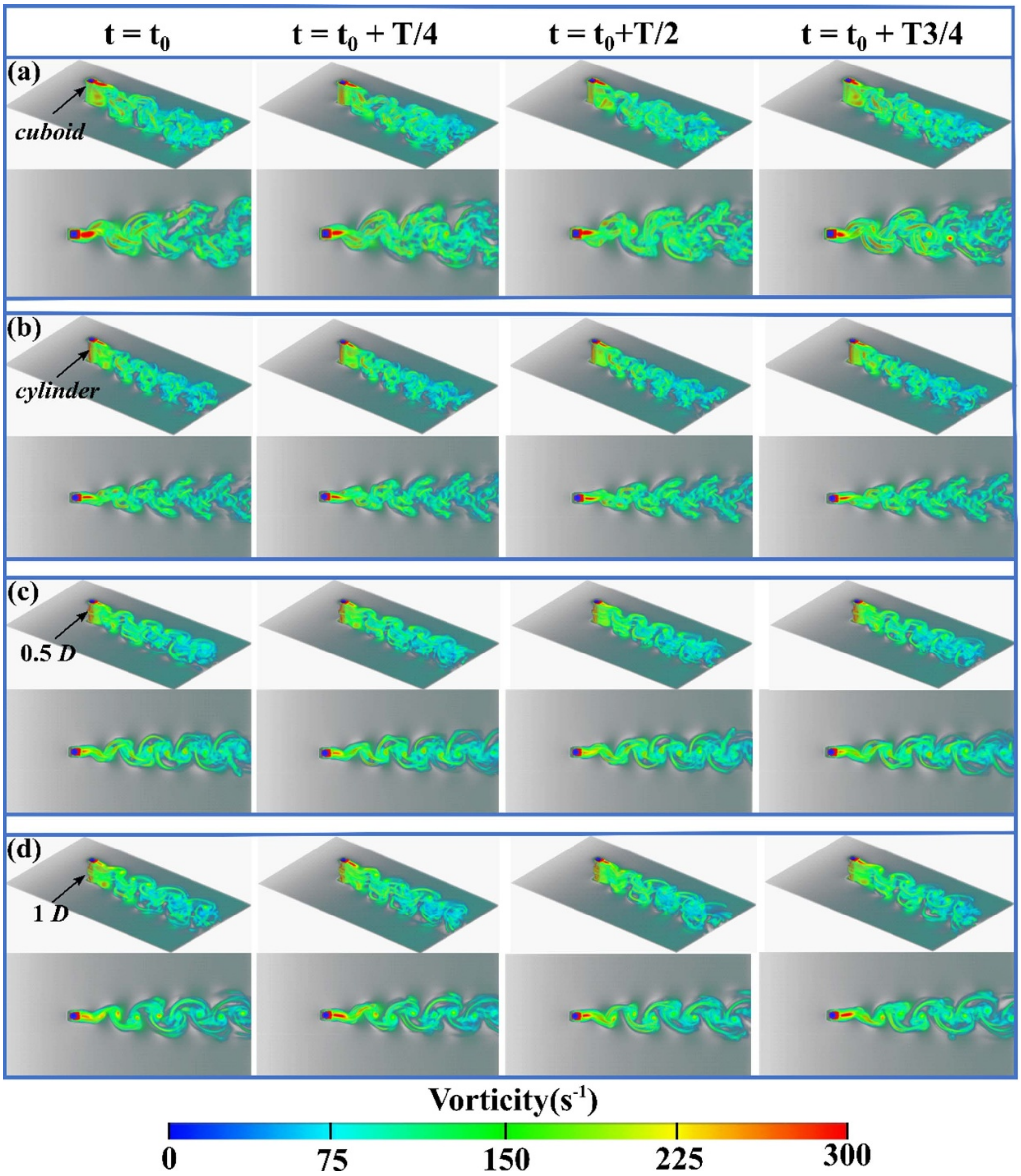

Figure 9. Vorticity contours obtained by CFD simulation at a wind speed 2.646 m s^{-1}: (a) cuboid; (b) cylinder; (c) 0.5D; and (d) 1D bluff bodies.

body is apparently less dispersed. This explains why the 1D FIV-PEH produced a larger voltage output, as shown in the results in figure 5. In a word, it is revealed that introducing hybridization into bluff bodies changes the vorticity flow behind them and alters the vortex-shedding behavior. The vortex-shedding effect, in turn, affects the vibration of the bluff body, as well as the performance of the harvester.

5. Conclusion

This study has attempted to induce the galloping-VIV coupling phenomenon to benefit small-scale wind energy harvesting by using a hybridized bluff body. The proposed hybridized bluff body constitutes of two cylindrical segments and one cuboid segment. Six hybridized bluff bodies with different cuboid segment lengths ($L = 0.5D$, $1D$, $1.5D$, $2D$, $2.5D$, and $3D$) were fabricated. $D = 32$ mm is the diameter of the cylindrical segment. The experimental results indicated that, when $L = 0.5D$, $1D$, the hybridized bluff body exhibits VIV in the low wind-speed range and galloping in the high wind-speed range. The galloping-VIV coupling phenomenon appears in the medium wind-speed range. It is found that the 1D FIV-PEH has a lower cut-in wind speed than the baseline G-PEH. Moreover, the voltage output amplitude of the 1D FIV-PEH is always at the intermediate level in both the low- and high-speed ranges compared to the two baseline models. Therefore, the 1D FIV-PEH can be deemed as quite a robust design.

However, if the cuboid segment length exceeds 1.5D, the galloping-VIV coupling phenomenon disappears. Consequently, the hybridized bluff body exhibits galloping-like motion over the whole wind-speed range. And, unfortunately, compared to the baseline G-PEH, the cut-in wind speed of the hybridized bluff body is marginally increased, and the voltage output amplitude is slightly decreased. From the above results, one knows that the length of the cuboid segment should be designed to be relatively small. In this way, the cylindrical segments play the dominant role in the low wind-speed range, making the system carry on VIV; and the cuboid segment plays the dominant role in the high wind-speed range, making the system carry on galloping.

In addition to the experiments, CFD simulations were conducted to investigate the aerodynamics of the bluff bodies. In general, the vorticity flow is changed for the hybridized bluff body. An obvious vortex-shedding effect forms behind the hybridized bluff body with a cuboid segment length of 1D at a wind speed of 2.646 m s^{-1}. This, in turn, affects the vibration of the bluff body and the voltage output response of the piezoelectric transducer attached to the system.

Data availability statement

All data that support the findings of this study are included within the article (and any supplementary files).

Acknowledgments

This work was supported by the National Natural Science Foundation of China (Grant No. 51977196) and the Henan Province Science Foundation for Youths (202300410422).

ORCID iDs

Junlei Wang https://orcid.org/0000-0003-4453-0946
Guobiao Hu https://orcid.org/0000-0002-1288-7564

References

[1] Rahman M M, Oni A O, Gemechu E and Kumar A 2020 Assessment of energy storage technologies: a review *Energy Convers. Manage.* **223** 113295

[2] Koohi-Fayegh S and Rosen M A 2020 A review of energy storage types, applications and recent developments *J. Energy Storage* **27** 101047

[3] Gur T M 2018 Review of electrical energy storage technologies, materials and systems: challenges and prospects for large-scale grid storage *Energy Environ. Sci.* **11** 3055

[4] Fang S, Wang S, Zhou S, Yang Z and Liao W-H 2020 Analytical and experimental investigation of the centrifugal softening and stiffening effects in rotational energy harvesting *J. Sound Vib.* **488** 115643

[5] Ma X and Zhou S 2022 A review of flow-induced vibration energy harvesters *Energy Convers. Manage.* **254** 115223

[6] Li Z, Zhou S and Yang Z 2022 Recent progress on flutter-based wind energy harvesting *Int. J. Mech. Syst. Dyn.* **2** 82–98

[7] Wang H Z, Lei Z X, Zhang X, Zhou B and Peng J C 2019 A review of deep learning for renewable energy forecasting *Energy Convers. Manage.* **198** 111799

[8] Owusu P A and Asumadu-Sarkodie S 2016 A review of renewable energy sources, sustainability issues and climate change mitigation *Cogent Eng.* **3** 1167990

[9] Salame C T 2020 Technologies and materials for renewable energy, environment and sustainability *Energy Rep.* **6** 1–3

[10] Wang J L, Tang L H, Zhao L Y, Hu G B, Song R J and Xu K 2020 Equivalent circuit representation of a vortex-induced vibration-based energy harvester using a semi-empirical lumped parameter approach *Int. J. Energy Res.* **44** 4516–28

[11] Pan H Y, Li H, Zhang T S, Laghari A A, Zhang Z T, Yuan Y P and Qian B 2019 A portable renewable wind energy harvesting system integrated S-rotor and H-rotor for self-powered applications in high-speed railway tunnels *Energy Convers. Manage.* **196** 56–68

[12] Rostami A B and Armandei M 2017 Renewable energy harvesting by vortex-induced motions: review and benchmarking of technologies *Renew. Sustain. Energy Rev.* **70** 193–214

[13] Iqbal M, Nauman M M, Khan F U, Abas P E, Cheok Q, Iqbal A and Aissa B 2021 Vibration-based piezoelectric, electromagnetic, and hybrid energy harvesters for microsystems applications: a contributed review *Int. J. Energy Res.* **45** 65–102

[14] Wang J L, Geng L F, Ding L, Zhu H J and Yurchenko D 2020 The state-of-the-art review on energy harvesting from flow-induced vibrations *Appl. Energy* **267** 114902

[15] Zhang L B, Abdelkefi A, Dai H L, Naseer R and Wang L 2017 Design and experimental analysis of broadband energy harvesting from vortex-induced vibrations *J. Sound Vib.* **408** 210–19

[16] Wang J L, Zhao W, Su Z, Zhang G J, Li P and Yurchenko D 2020 Enhancing vortex-induced vibrations of a cylinder with rod attachments for hydrokinetic power generation *Mech. Syst. Signal Process.* **145** 106912

[17] Dai H L, Abdelkefi A and Wang L 2017 Vortex-induced vibrations mitigation through a nonlinear energy sink *Commun. Nonlinear Sci. Numer. Simul.* **42** 22–36

[18] Wang J L, Geng L F, Zhou S X, Zhang Z E, Lai Z H and Yurchenko D 2020 Design, modeling and experiments of broadband tristable galloping piezoelectric energy harvester *Acta Mech. Sin.* **36** 592–605

[19] Wang J L, Tang L H, Zhao L Y and Zhang Z 2019 Efficiency investigation on energy harvesting from airflows in HVAC system based on galloping of isosceles triangle sectioned bluff bodies *Energy* **172** 1066–78

[20] Tan T, Hu X Y, Yan Z M and Zhang W M 2019 Enhanced low-velocity wind energy harvesting from transverse galloping with super capacitor *Energy* **187** 115915

[21] Liu J J, Zuo H, Xia W, Luo Y J, Yao D, Chen Y J, Wang K and Li Q 2020 Wind energy harvesting using piezoelectric macro fiber composites based on flutter mode *Microelectron. Eng.* **231** 111333

[22] Li Z, Zhou S and Li X 2022 A piezoelectric–electromagnetic hybrid flutter-based wind energy harvester: modeling and nonlinear analysis *Int. J. Nonlinear Mech.* **144** 104051

[23] Hasheminejad S M, Rabiee A H and Markazi A H D 2018 Dual-functional electromagnetic energy harvesting and vortex-induced vibration control of an elastically mounted circular cylinder *J. Eng. Mech.* **144** 04017184

[24] Zhang C Y, Hu G, Yurchenko D, Lin P F, Gu S H, Song D R, Peng H Y and Wang J L 2021 Machine learning based prediction of piezoelectric energy harvesting from wake galloping *Mech. Syst. Signal Process.* **160** 107876

[25] Wang J L, Gu S H, Abdelkefi A, Zhang M J, Xu W H and Lai Y Y 2021 Piezoelectric energy harvesting from flow-induced vibrations of a square cylinder at various angles of attack *Smart Mater. Struct.* **30** 08LT02

[26] Fang S, Miao G, Chen K, Xing J, Zhou S, Yang Z and Liao W-H 2022 Broadband energy harvester for low-frequency rotations utilizing centrifugal softening piezoelectric beam array *Energy* **241** 122833

[27] Lai Z H, Wang S B, Zhu L K, Zhang G Q, Wang J L, Yang K and Yurchenko D 2021 A hybrid piezo-dielectric wind energy harvester for high-performance vortex-induced vibration energy harvesting *Mech. Syst. Signal Process.* **150** 107212

[28] Zeng Q X *et al* 2020 A high-efficient breeze energy harvester utilizing a full-packaged triboelectric nanogenerator based on flow-induced vibration *Nano Energy* **70** 104524

[29] Xin C, Li Z, Zhang Q, Peng Y, Guo H and Xie S 2022 Investigating the output performance of triboelectric nanogenerators with single/double-sided interlayer *Nano Energy* **100** 107448

[30] Mutsuda H, Tanaka Y, Patel R and Doi Y 2017 Harvesting flow-induced vibration using a highly flexible piezoelectric energy device *Appl. Ocean Res.* **68** 39–52

[31] Adhikari S, Friswell M I and Inman D J 2009 Piezoelectric energy harvesting from broadband random vibrations *Smart Mater. Struct.* **18** 115005

[32] Anton S R and Sodano H A 2007 A review of power harvesting using piezoelectric materials (2003–2006) *Smart Mater. Struct.* **16** R1–R21

[33] Zhang M, Hu G B and Wang J L 2020 Bluff body with built-in piezoelectric cantilever for flow-induced energy harvesting *Int. J. Energy Res.* **44** 3762–77

[34] Abdelkefi A, Najar F, Nayfeh A H and Ben Ayed S 2011 An energy harvester using piezoelectric cantilever beams undergoing coupled bending-torsion vibrations *Smart Mater. Struct.* **20** 115007

[35] Zhang G C, Klumpner C and Lin Y J 2019 Energy harvesting utilizing reciprocating flow-induced torsional vibration on a T-shaped cantilever beam *Smart Mater. Struct.* **28** 025001

[36] Dash R C, Maiti D K and Singh B N 2021 A finite element model to analyze the dynamic characteristics of galloping based piezoelectric energy harvester *Mech. Adv. Mater. Struct.* 1–14 accepted

[37] Huo B, Li X L, Cui F J, Yang S and Nascimbene R 2021 Theoretical analysis and experimental validation on galloping of iced transmission lines in a moderating airflow *Shock Vib.* **2021** 1–12

[38] Gabbai R D and Benaroya H 2005 An overview of modeling and experiments of vortex-induced vibration of circular cylinders *J. Sound Vib.* **282** 575–616

[39] Pan F F, Xu Z K, Pan P and Jin L 2017 Piezoelectric energy harvesting from vortex-induced vibration using a modified circular cylinder *2017 20th Int. Conf. on Electrical Machines and Systems (ICEMS)*

[40] Wang J L, Zhou S X, Zhang Z E and Yurchenko D 2019 High-performance piezoelectric wind energy harvester with Y-shaped attachments *Energy Convers. Manage.* **181** 645–52

[41] Wang J L, Zhang C Y, Zhang M J, Abdelkefi A, Yu H Y, Ge X M and Liu H D 2021 Enhancing energy harvesting from flow-induced vibrations of a circular cylinder using a downstream rectangular plate: an experimental study *Int. J. Mech. Sci.* **211** 106781

[42] Wang J, Gu S, Abdelkefi A and Bose C 2021 Enhancing piezoelectric energy harvesting from the flow-induced vibration of a circular cylinder using dual splitters *Smart Mater. Struct.* **30** 08LT02

[43] Yu H Y and Zhang M J 2021 Effects of side ratio on energy harvesting from transverse galloping of a rectangular cylinder *Energy* **226** 120420

[44] Abdelkefi A, Yan Z M and Hajj M R 2013 Modeling and nonlinear analysis of piezoelectric energy harvesting from transverse galloping *Smart Mater. Struct.* **22** 025016

[45] Zhao L Y, Tang L H and Yang Y W 2012 Small wind energy harvesting from galloping using piezoelectric materials *Proc. ASME Conf. on Smart Materials, Adaptive Structures and Intelligent Systems* vol 2 pp 919–27

[46] Wang J L, Zhang C Y, Gu S H, Yang K, Li H, Lai Y Y and Yurchenko D 2020 Enhancement of low-speed piezoelectric wind energy harvesting by bluff body shapes: spindle-like and butterfly-like cross-sections *Aerosp. Sci. Technol.* **103** 105898

[47] Tan T, Zuo L and Yan Z M 2021 Environment coupled piezoelectric galloping wind energy harvesting *Sens. Actuators* A **323** 112641

[48] Zhao D L, Hu X Y, Tan T, Yan Z M and Zhang W M 2020 Piezoelectric galloping energy harvesting enhanced by topological equivalent aerodynamic design *Energy Convers. Manage.* **222** 113260

[49] Mannini C, Marra A M, Massai T and Bartoli G 2016 Interference of vortex-induced vibration and transverse galloping for a rectangular cylinder *J. Fluids Struct.* **66** 403–23

[50] Liu Y Z, Ma C M, Li Q S, Yan B W and Liao H L 2018 A new modeling approach for transversely oscillating square-section cylinders *J. Fluids Struct.* **81** 492–513